Article

Molecular Order Control of Non-fullerene Acceptors for High-Efficiency Polymer Solar Cells

Wei Li, Mengxue Chen, Jinlong Cai, ..., David G. Lidzey, Liming Ding, Tao Wang

ding@nanoctr.cn (L.D.)
twang@whut.edu.cn (T.W.)

HIGHLIGHTS

COi8DFIC lamellae can be converted to H- and J-type π-π stacks by hot-substrate casting

H- and J-type π-π stacking broadens the absorption spectrum of COi8DFIC molecules

Same orientation of donor and acceptor promotes charge generation

Binary PTB7-Th:COi8DFIC solar cell achieves a maximum efficiency of 13.8%

Tuning the molecular ordering of COi8DFIC from flat-on and edge-on lamellae to H- and J-type π-π stacking results in broadened absorption spectrum and fine phase separation with the electron donor PTB7-Th, which promotes efficient exciton dissociation at the donor/acceptor interface together with enhanced and balanced carrier mobility, and leads to an unprecedented PCE of 13.8% of single-junction, binary PTB7-Th:COi8DFIC solar cell.

Article

Molecular Order Control of Non-fullerene Acceptors for High-Efficiency Polymer Solar Cells

Wei Li,[1,2] Mengxue Chen,[1,2] Jinlong Cai,[1,2] Emma L.K. Spooner,[3] Huijun Zhang,[1,2] Robert S. Gurney,[1,2] Dan Liu,[1,2] Zuo Xiao,[4] David G. Lidzey,[3] Liming Ding,[4,*] and Tao Wang[1,2,5,*]

SUMMARY

Adjusting molecular ordering, orientation, and nanoscale morphology within the photoactive layer of polymer:non-fullerene organic solar cells is crucial in achieving high power-conversion efficiency (PCE). Herein, we demonstrate that the molecular ordering and orientation of the n-type small-molecule acceptor COi8DFIC can be tuned from flat-on and edge-on lamellar crystalline to H- and J-type π-π stacking during the solution-casting process, resulting in broadened photon absorption and fine phase separation with the electron donor PTB7-Th. This favorable morphology with face-on π-π stacked electron donors and acceptors promotes efficient exciton dissociation at the donor/acceptor interface, together with enhanced and balanced carrier mobility. The enhanced short-circuit current density and fill factor lead to the achievement of a maximum PCE of 13.8% in binary, single-junction PTB7-Th:COi8DFIC non-fullerene polymer solar cells while also exhibiting superior stability.

INTRODUCTION

Non-fullerene small-molecule electron acceptors (NFAs) have attracted considerable attention and promoted encouraging progress of organic photovoltaics (OPVs) in recent years.[1–6] NFAs possess considerable advantages over their fullerene counterparts, including tunable bandgaps and energy levels as well as the ability to achieve efficient exciton separation with the presence of a dramatically reduced energy offset between electron donors and NFAs.[7,8] The maximum achievable power-conversion efficiency (PCE) of non-fullerene OPVs has reached over 14% in single-junction binary devices,[9] outperforming any fullerene-based OPVs reported in the literature.[10]

The morphological configurations of electron donor and electron acceptor are critical in bulk heterojunction OPVs.[11,12] Factors such as domain size, domain purity, and molecular order of the electron donor or acceptor component are strongly associated with the exciton dissociation and charge-transport processes of OPVs and directly influence their device performance.[13–15] One of the most important factors is the molecular orientation of donors and acceptors with respect to the electrodes, which is essential to carrier transport in the vertical direction, and also influences the π-π interactions between them that affect charge separation.[16,17] Fullerene acceptors always exhibit isotropic molecular orientation (i.e., they do not have edge-on or face-on orientations) due to their sphere-like structures, with only their aggregation dimensionality adjustable. In polymer-fullerene systems, this restricts the tunability of the orientation, in particular π-π interactions

Context & Scale

The increasing use of non-fullerene electron acceptors (NFAs) is boosting the power-conversion efficiency (PCE) of organic photovoltaics (OPVs). This benefits from the merits of NFAs including tunable bandgaps and energy levels, and efficient exciton separation upon a small energy offset. The versatile structures of NFAs also bring vastly different molecular ordering and orientation behaviors, which in turn affect their light absorption, phase separation with donors, exciton splitting, and ultimately device PCE. The emergence of NFAs therefore not only offers a promising approach to preparing high-performance OPVs but also requires fundamental understanding of the relationship between molecular morphology and PCE. Here, the molecular ordering and orientation of COi8DFIC are tuned during solution casting from flat-on and edge-on lamellae to H- and J-type π-π stacking, which broadens the absorption spectrum, improves exciton dissociation, and enhances electron mobility toward improvement of device PCE.

between polymer and fullerene, which can only be amended through the orientation of polymer donors.[18,19]

On the other hand, the molecular structure of NFAs can be designed, forming either rigid and planar structure (e.g., perylene diimide-based NFAs) [20,21] or bulky and twisted structure (e.g., ladder-type aromatic cores-based NFAs), which renders them different trends of molecular organization behavior during the solution-casting process.[22] Although this anisotropic molecular orientation characteristic of NFAs confers infinite possibilities to tune the bulk heterojunction morphology of the polymer:non-fullerene active layer, it also requires strict selectivity of suitable electron donors with favorable molecular order[22,23] or suitable molecular weight[24] to achieve the best performance.[25] Indeed, the conjugated molecular structure of NFAs brings challenges to prepare high-performing OPVs, but also builds a promising platform to achieve higher device efficiency by rational control of molecular ordering and nanoscale phase separation in the non-fullerene OPVs.[26]

Recently a novel NFA, CO*i*8DFIC, has emerged and been demonstrated to obtain a high PCE of 12.1% in single-junction binary solar cells,[27] 14.6% in single-junction ternary devices,[28,29] and over 17% in two-terminal tandem devices.[30] In this work, we report a novel approach to improve solar cell efficiency via control of the molecular ordering of CO*i*8DFIC in its binary photovoltaic blend with poly([2,6'-4,8-di(5-dethylhexylthienyl)benzo[1,2-b; 3,3-b] dithiophene]{3-fluoro-2[(2- ethylhexyl) carbonyl]thieno[3,4-b]thiophenediyl}) (PTB7-Th). Herein, the molecular ordering of CO*i*8DFIC is manipulated to be either crystalline or H- and J-type π-π stacking, by increasing the molecular organization time via solvent-vapor annealing (SA) after film-casting or by reducing the molecular organization time via film-casting on hot substrate (HS). We show that lamellar crystalline CO*i*8DFIC molecules present reduced photon absorption ability with a narrow spectrum range, while π-π stacked CO*i*8DFIC molecules present enhanced absorption in a broadened spectrum range. The crystallized photovoltaic blend films exhibit a large spacing of at least 1.0 nm between the conjugated backbones of CO*i*8DFIC molecules, while much denser π-π stacks with a separation space of 0.39 nm exist in the CO*i*8DFIC domains of films processed via HS casting. This leads to the broadening of the external quantum efficiency (EQE) spectrum from 900 to 1,050 nm, contributing to a maximum short-circuit current (J_{sc}) of 28.3 mA cm^{-2}, fill factor (FF) of 0.71, open-circuit voltage (V_{oc}) of 0.69 V, and PCE of 13.8% in PTB7-Th:CO*i*8DFIC binary solar cells.

RESULTS AND DISCUSSION

Molecular Ordering and Orientation of CO*i*8DFIC

The chemical structures and energy levels of the electron donor PTB7-Th and electron acceptor CO*i*8DFIC studied in this work are shown in Figures 1A and 1B. The highest occupied molecular orbital and lowest unoccupied molecular orbital level of CO*i*8DFIC are −5.50 and −3.88 eV, respectively.[28] The A-D-A type CO*i*8DFIC molecule possesses eight fused rings in the D domain, and two difluoro-substituted end groups referred to as A domains. The enhanced planarity of CO*i*8DFIC grants it high crystallization ability during the solution-casting process.

When processing CO*i*8DFIC molecules at room temperature (RT) using a conventional solvent, for example chlorobenzene (CB), they show strong self-organization behavior and form crystallites. The resulting films (see Figures 2A and 2B) present lamellar-like aggregates with poor surface coverage due to the presence of large

[1]State Key Laboratory of Silicate Materials for Architectures, Wuhan University of Technology, Wuhan 430070, China

[2]School of Materials Science and Engineering, Wuhan University of Technology, Wuhan 430070, China
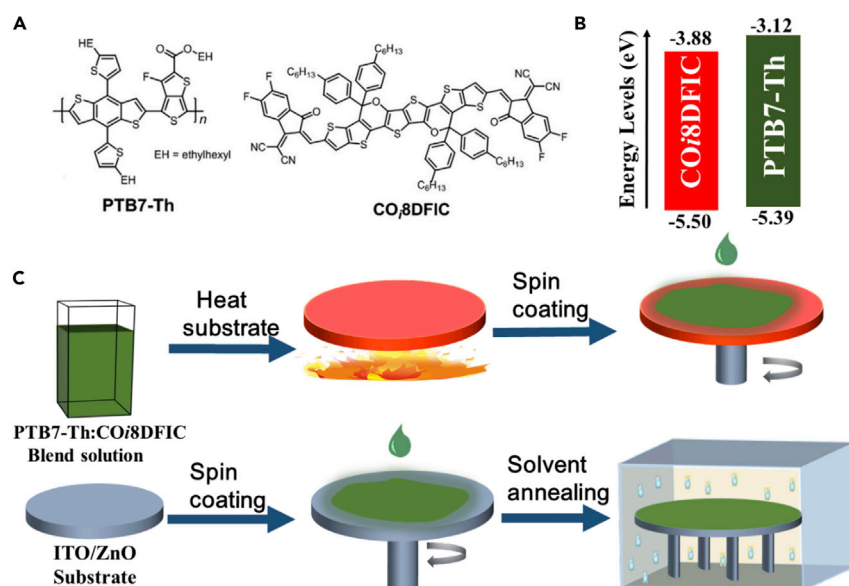
[3]Department of Physics and Astronomy, University of Sheffield, Sheffield S3 7RH, UK

[4]Center for Excellence in Nanoscience (CAS), Key Laboratory of Nanosystem and Hierarchical Fabrication (CAS), National Center for Nanoscience and Technology, Beijing 100190, China

[5]Lead Contact

*Correspondence: ding@nanoctr.cn (L.D.), twang@whut.edu.cn (T.W.)

Figure 1. Chemical Structures, Energy Levels of PTB7-Th and COi8DFIC, and Schematic of Film-Casting on a Hot Substrate and a Spin-Cast Film Undergoing Solvent-Vapor Annealing

(A) Chemical structures of PTB7-Th and COi8DFIC.

(B) Energy levels of PTB7-Th and COi8DFIC.

(C) Schematic of film-casting on a hot substrate (HS) and a spin-cast film undergoing solvent-vapor annealing (SA).

crystallites. Grazing-incidence wide-angle X-ray scattering (GIWAXS) characterization (Figures 2E, 2F, and S1) of a COi8DFIC film cast at RT exhibits numerous sharp diffraction rings located from 0.5 to 2 Å^{-1} in both in-plane and out-of-plane directions, suggesting that COi8DFIC molecules are highly crystallized. The diffraction rings locating at q_z of 0.62, 1.24, and 1.86 Å^{-1} are preferentially stronger in the out-of-plane direction, and are indexed as the (001), (002), and (003) diffraction peaks of flat-on lamella crystalline of COi8DFIC backbone,[31] while the diffraction peak at q_z = 1.6 Å^{-1} is attributed to the (010) π-π stacking within COi8DFIC crystals. Moreover, the intensity of (001) diffraction peak is much stronger than all other diffraction peaks, suggestion that flat-on backbone orientation dominates the molecular orientation in the pure COi8DFIC film. However, when the COi8DFIC film is cast on a substrate previously held at a temperature of 100°C, the resulting film is uniform and homogeneous (see Figures 2C and 2D). The GIWAXS result of this COi8DFIC film cast on the 100°C HS shows that the intensity of its diffraction rings reduces significantly, suggesting the decrease of crystalline order in the film. Compared with the film cast at RT, the solvent evaporation rate will be significantly higher by casting on the 100°C HS, therefore reducing the film-drying time. This accelerated film-formation process will inhibit the self-organization of COi8DFIC molecules into crystallites. As an extreme and opposite case where self-organization of COi8DFIC molecules is encouraged, the RT-cast COi8DFIC film was further treated using a solvent-vapor annealing approach, during which the molecules will become active again and can reorganize into crystallites.[32,33] Intuitively, COi8DFIC film with further SA treatment exhibits the strongest crystallinity, evidenced by the fact that the diffraction rings in both in-plane or out-of-plane become most pronounced (see Figure S1). Overall, our results suggest that the crystallinity of COi8DFIC can be manipulated by controlling the film-drying time during solution casting.
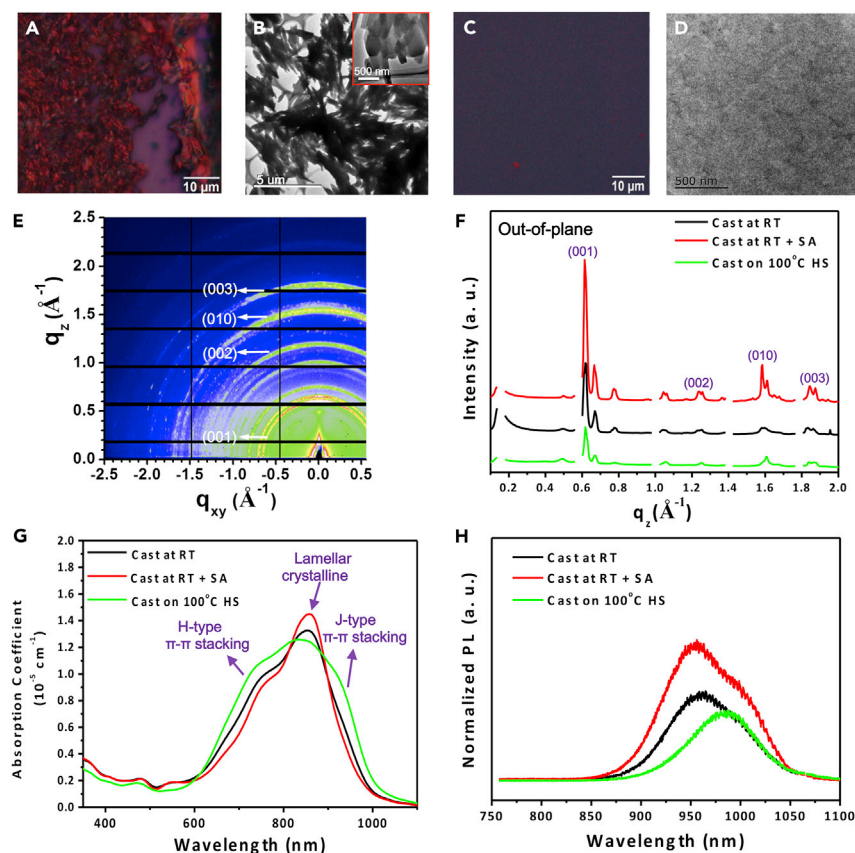
Figure 2. Optical Microscope Surface Images, TEM Images, GIWAXS, Absorption Spectra, and PL Spectra of Pure COi8DFIC Films Cast at RT, at RT with SA, or on 100°C HS

(A) Optical microscope surface image of pure COi8DFIC film cast at RT.

(B) TEM image of COi8DFIC film cast at RT.

(C) Optical microscope surface image of pure COi8DFIC film cast on 100°C HS.

(D) TEM image of COi8DFIC film cast on 100°C HS.

(E) 2D GIWAXS pattern of pure COi8DFIC film cast at RT.

(F) Out-of-plane 1D profiles of GIWAXS along q_z axis for pure COi8DFIC films cast at RT, at RT + SA, or on 100°C HS.

(G) Absorption spectra of COi8DFIC films cast at RT, at RT + SA, or on 100°C HS.

(H) PL spectra of COi8DFIC films cast at RT, at RT + SA, or on 100°C HS.

Figure 2G shows the absorption spectra of COi8DFIC films cast at RT, at RT with SA, and on 100°C HS. The COi8DFIC film containing flat-on dominated lamellar crystallites exhibits a primary peak at 850 nm. With the crystallinity of COi8DFIC decreasing this primary peak stays at 850 nm, but the absorption spectrum becomes broader. When the COi8DFIC film is cast on 100°C HS, the broadening of the absorption spectrum is most pronounced. We attribute the blue shift of the spectrum to the H-type π-π stacking of COi8DFIC, and the red shift of the spectrum to the J-type π-π stacking of COi8DFIC.[34,35] The red shift of the COi8DFIC absorption spectrum also suggests that the bandgap of COi8DFIC has been shortened, which is in line with the red shift of the photoluminescence (PL) spectrum, as shown in Figure 2H. Consequently, this suppressed crystallization of COi8DFIC encourages both H- and J-type π-π stacking to broaden the photon absorption range of the photoactive layer, and in principle will increase the PCE of the non-fullerene OPV device if efficient charge separation and collection can be granted.
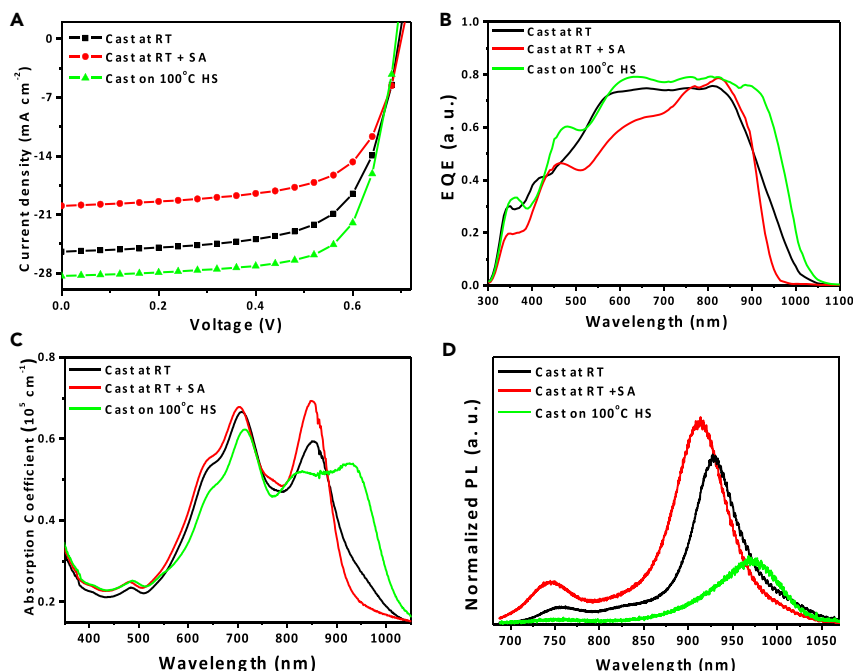
Figure 3. Device Characteristics and EQE of PTB7-Th:COi8DFIC OPV Devices, and Absorption Spectra and PL Spectra of PTB7-Th:COi8DFIC Blend Films

(A and B) Champion *J-V* curves (A) and EQE (B) of PTB7-Th:COi8DFIC devices upon varying film preparation conditions.

(C and D) Absorption (C) and PL (D) spectra of PTB7-Th:COi8DFIC films cast at RT, at RT + SA, or on 100°C HS.

Device Performance of PTB7-Th:COi8DFIC Solar Cells

We then fabricated OPV devices (indium tin oxide [ITO]/ZnO/PTB7-Th:COi8DFIC/MoO$_3$/Ag) by incorporating PTB7-Th:COi8DFIC photovoltaic blends as the photoactive layer, which was cast at RT, at RT with SA, or on HS to allow different molecular ordering of COi8DFIC within the photoactive layer. Figure 3A shows the current density versus voltage (*J-V*) characteristics of PTB7-Th:COi8DFIC devices with the active layer having been processed at various conditions. The blend film cast at RT gave an average PCE of 11.2% (with PCE$_{max}$ at 11.7%), with an average V_{oc} of 0.69 V, J_{sc} of 24.8 mA cm^{-2}, and FF of 66%. After SA treatment, although its FF and V_{oc} stayed almost unchanged, the average J_{sc} of the device decreased dramatically to 19.9 mA cm^{-2} and obtained an average PCE of 9.0% (with PCE$_{max}$ at 9.3%). On the contrary, when the active layer was cast on 100°C HS to accelerate the solvent evaporation rate, the device average J_{sc} increased from 24.8 to 27.3 mA cm^{-2} and the FF was improved to over 70%. These improved J_{sc} and FF result in an 18% enhancement in PCE$_{max}$ from 11.7% to 13.8% (with the efficiency distribution shown in Figure S2), which is an unprecedented PCE for single-junction, binary PTB7-Th:COi8DFIC OPVs, demonstrating the effectiveness of increase the device efficiency by reducing the film-drying time.[36,37] An improvement from 11.7% to 12.8% PCE$_{max}$ was also achieved by casting the film on 50°C HS, mainly via the enhancements of J_{sc} and FF (see the summary in Table 1). When the film was cast on 70°C HS, the device PCE$_{max}$ could be further increased to 13.2%. However, when film was cast on 150°C HS, a reduced PCE$_{max}$ of 11.0% resulted, through reductions in FF and J_{sc}. The optimum substrate temperature was therefore determined at 100°C.

**Table 1. Summary of Photovoltaic Parameters of PTB7-Th:COi8DFIC OPVs Measured at an Illumination of AM 1.5G at 100 mW cm^{-2}**

PTB7-Th:COi8DFIC	FF (%)	J_{sc} (mA cm^{-2})	Calculated J_{sc} (mA cm^{-2})	V_{oc} (V)	PCE$_{avg}$ (%)	PCE$_{max}$ (%)
Cast at RT	66 ± 0.6	24.8 ± 0.4	23.4	0.69 ± 0.002	11.2 ± 0.2	11.7
Cast at RT + SA	65 ± 0.8	19.9 ± 0.9	19.7	0.70 ± 0.002	9.0 ± 0.3	9.3
Cast on 50°C HS	70 ± 1.0	25.8 ± 0.4	24.9	0.69 ± 0.002	12.5 ± 0.2	12.8
Cast on 70°C HS	71 ± 0.7	26.2 ± 0.3	25.6	0.69 ± 0.002	12.9 ± 0.2	13.2
Cast on 100°C HS	71 ± 1.0	27.3 ± 0.5	26.5	0.69 ± 0.002	13.4 ± 0.2	13.8
Cast on 150°C HS	61 ± 1.0	24.5 ± 0.5	23.4	0.70 ± 0.002	10.6 ± 0.3	11.0

The statistical data presented were obtained from over 40 individual devices.

EQE measurements were used to characterize the range and magnitude of the spectral response of these OPVs. As shown in Table 1 and Figure 3B, the calculated J_{sc} from EQE spectra are only ca. 5% less than the J_{sc} values obtained from our J-V scans, and therefore confirms the validity of our J-V measurements. Moreover, the device cast at RT exhibits a strong spectral response ranging from 300 to 1,000 nm, in line with previous work.[27,28] After further treatment with SA, the EQE spectrum shows a blue shift with the optical absorption edge reducing from ca. 1,050 to 950 nm, and a notable intensity decline in the range from 300 to 800 nm. The fact that light absorption from 300 to 800 nm has not been affected (see Figure 3C) indicates inefficient exciton dissociation between PTB7-Th and COi8DFIC. We attribute this to the enlarged domain size, and different orientations of donor and acceptor, i.e., face-on packing for PTB7-Th and flat-on and edge-on packing for COi8DFIC, in the photoactive layer, which hinder exciton dissociation at their interface (see next section for morphology characteristics). When the photoactive layer of the device was cast on 100°C HS, while the EQE intensity increased slightly in the wavelength range from 300 to 900 nm, it increased dramatically from 900 to 1,050 nm. The enhanced J_{sc} of OPVs device cast on 100°C HS can be attributed to the improved photon absorption (see Figure 3C) and photon-to-carrier conversion in the spectral range between 900 and 1,050 nm. The primary PL peak (see Figure 3D) of the blend film cast at RT located at 930 nm, and was blue-shifted to 910 nm after further SA treatment and red-shifted to 975 nm when casting on 100°C HS, observations further confirm that the bandgap of COi8DFIC in PTB7-Th:COi8DFIC blend has been affected by the different molecular order of COi8DFIC. Compared with the film cast at RT, the film with further SA treatment exhibits enhanced PL density (see the primary peak and the PL emission peak of PTB7-Th at 750 nm), while the film cast on 100°C HS exhibits reduced PL density. These indicate a reduced PL quenching effect in the SA-treated film due to enlarged domain size and an enhanced PL quenching effect in the HS-cast film due to intimate mixing of donors and acceptors, characteristics that we present in the following section.

Nanoscale Morphology of PTB7-Th:COi8DFIC Photovoltaic Blends

The domain sizes of PTB7-Th and COi8DFIC in the films processed at varying conditions were firstly evaluated via scanning probe microscopy (SPM) and transmission electron microscopy (TEM). As shown in Figures 4A and 4D, the PTB7-Th:COi8DFIC blend film cast at RT exhibits medium phase separation, with a root-mean-square (RMS) surface roughness of 5.0 nm due to the existence of numerous aggregates with large aspect ratio. These aggregates appear white in the SPM image, and can be assigned to the COi8DFIC crystals formed during the solution-casting process. When the film was further treated with SA, these COi8DFIC crystals grew into large lamellar-like crystals (see Figures 4B and 4E), leading to a high RMS of 8.7 nm. These pronounced lamellar-like crystals formed in the blend film are similar
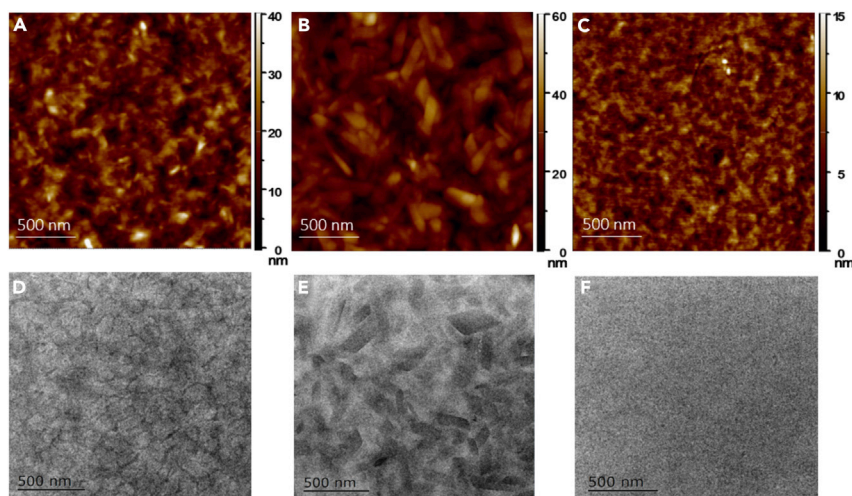
**Figure 4. SPM and TEM Images of PTB7-Th:CO*i*8DFIC Blend Films**
(A–C) SPM surface images of PTB7-Th:CO*i*8DFIC films cast (A) at RT, (B) at RT + SA, and (C) on 100°C HS.
(D–F) TEM images of PTB7-Th:CO*i*8DFIC films cast (D) at RT, (E) at RT + SA, and (F) on 100°C HS.

to those in pure CO*i*8DFIC film shown in Figure 1. This increases the phase separation between PTB7-Th, and is the origin of increased PL intensity of the SA-treated film illustrated in Figure 3D. Although these large crystals have the possibility to facilitate charge transport, the pronounced phase separation will also reduce the efficiency of free charge generation due to the reduced donor:acceptor interfacial area.[38] On the contrary, when the blend film was cast on 100°C HS, by kinetically inhibiting their growth during the solution-casting process the lamellar-like crystals almost completely disappeared. Fine phase separation can be observed in Figures 4C and 4F, and a low surface RMS roughness of 2.2 nm was observed.

To gain deeper insight into the molecular ordering within the PTB7-Th:CO*i*8DFIC films, we applied GIWAXS measurements. As shown in Figures S3A and S3B, pristine PTB7-Th presents an (010) peak at $q_z = 1.6$ Å^{-1} in the out-of-plane direction and a (100) peak at $q_{xy} = 0.28$ Å^{-1} in the in-plane direction, suggesting that PTB7-Th is largely amorphous with π-π stacking structure order, and is consistent with literature reports.[39] Figures 5A–5C show the 2D GIWAXS images of PTB7-Th:CO*i*8DFIC blend films, and Figures 5G and 5H plot their 1D profiles in the out-of-plane and in-plane directions. Figure 5G shows that the blend film cast at RT possesses moderate diffraction peak intensity, showing weak peak at $q_z = 0.62$ Å^{-1} that belongs to (001) backbone packing of CO*i*8DFIC, and weak peak at $q_z = 0.50$ Å^{-1} that belongs to alkyl chain packing of CO*i*8DFIC. These are associated with a d-space of 1.0 nm for backbone packing (obtained from d = 2π/q) and d-space of 1.3 nm for alkyl chain packing (see the scheme in Figure 5J). When the RT-cast blend film was further treated with SA, the backbone packing at $q_z = 0.62$ Å^{-1} became stronger, and the alkyl chain packing at $q_z = 0.50$ Å^{-1} also became pronounced, indicating the enhanced flat-on and edge-on molecular orientations. For the blend film cast on 100°C HS, the peaks at $q_z = 0.5$ Å^{-1} and 0.62 Å^{-1} were almost absent, suggesting the amorphous state of CO*i*8DFIC in the blend film. A broad diffraction crescent at $q_z = 1.6$–1.8 Å^{-1} in the out-of-plane direction was observed in Figure 5C, which is due to the convolution of π-π stacking peaks of PTB7-Th at $q_z = 1.6$ Å^{-1} and CO*i*8DFIC at $q_z = 1.6$ Å^{-1}. A much shorter separation space d = 0.39 nm between π-π stacks of CO*i*8DFIC molecules can be obtained via d = 2π/q. In the RT-cast
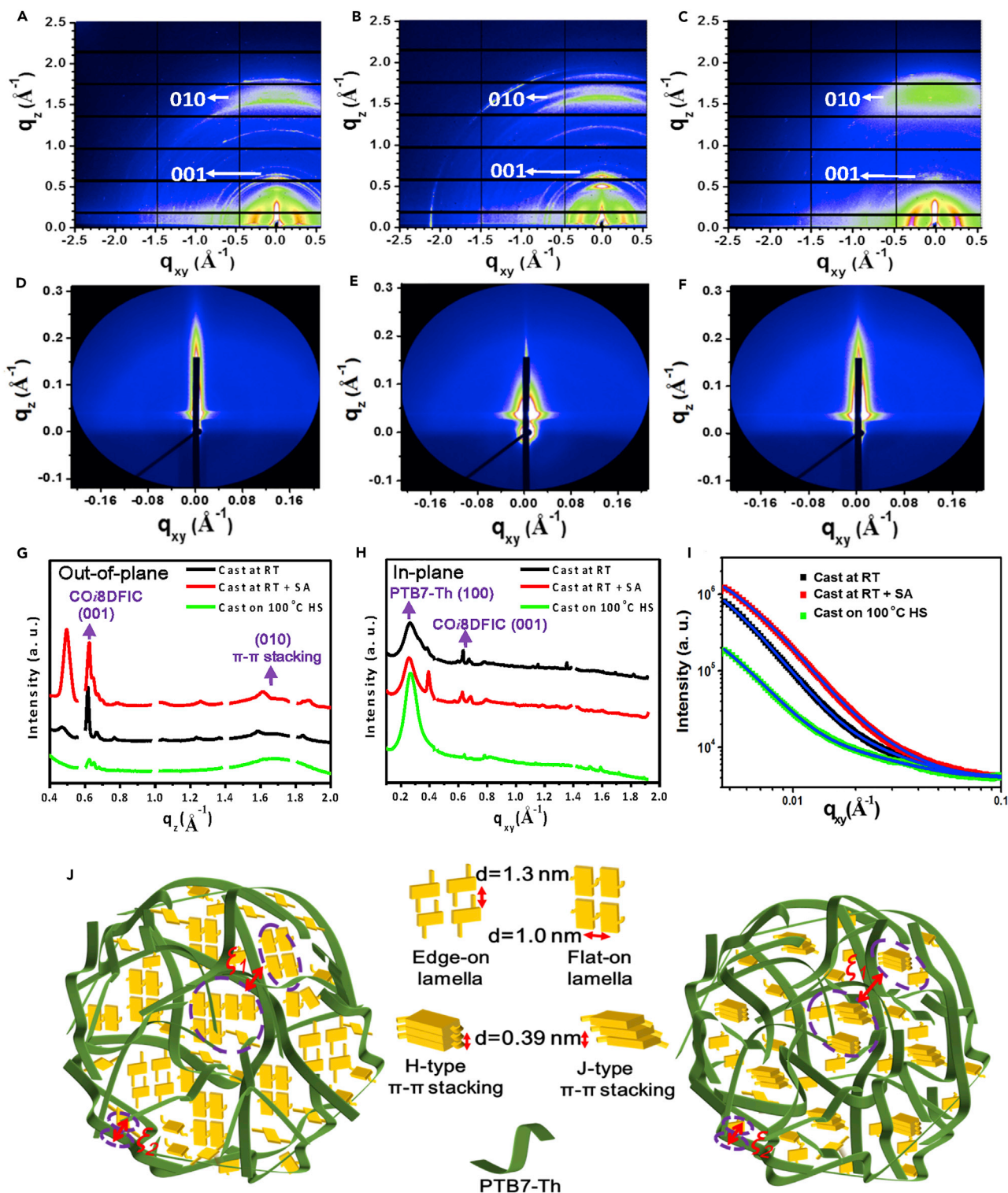
Figure 5. GIWAXS and GISAXS Results, and Schematic of Microstructures within PTB7-Th:COi8DFIC Films

(A–C) 2D GIWAXS of PTB7-Th:COi8DFIC films cast (A) at RT, (B) at RT + SA, and (C) on 100°C HS.

(D–F) 2D GISAXS of PTB7-Th:COi8DFIC films cast (D) at RT, (E) at RT + SA, and (F) on 100°C HS.

(G and H) Out-of-plane (G) and in-plane (H) 1D profiles of GIWAXS along q_z axis.

(I) In-plane 1D profiles of GISAXS along q_{xy} axis.

(J) Schematic of microstructures within PTB7-Th:COi8DFIC films: flat-on and edge-on lamellar crystalline, and H- and J-type π-π stacking of COi8DFIC.

and RT-cast blend film with SA treatment, PTB7-Th donors are largely face-on packed, while CO*i*8DFIC acceptors are edge-on and flat-on packed, different orientations that will hinder the intimate contact between donors and acceptors for efficient exciton splitting. In the blend film cast on 100°C, both PTB7-Th and CO*i*8DFIC are aligned face-on, allowing an intimate contact at their interface for efficient exciton splitting. The in-plane profiles in Figure 5H show that the structure order of PTB7-Th increases in blend cast on 100°C, implying that the suppressed crystallization of CO*i*8DFIC favors the molecular organization of PTB7-Th. It is generally accepted that π-π stacking along the out-of-plane direction (i.e., face-on π-π stacking) can provide ordered pathways for charge transport toward electrodes, a characteristic that is desired for high-performance OPVs.[40,41] Our GIWAXS results therefore conclude that in the blend film cast at RT and that subjected to further SA, CO*i*8DFIC molecules form an edge-on and flat-on lamellar crystalline structure with a separation distance of at least 1.0 nm, while forming H- and J-type π-π stacking with a short separation distance of 0.39 nm by casting on HS (see the scheme in Figure 5J). The H- and J-type π-π aggregations broaden the optical absorption of the device (see Figure 3C). In previous work, the absorption spectral range of OPVs was mainly altered by tuning the aggregation state of polymer donors via the temperature-dependent aggregation behavior of polymers.[42–44] The red shift or blue shift of optical absorption has not been reported so far via the control of H- and J-type aggregation of NFAs.

The nanoscale phase separation within PTB7-Th:CO*i*8DFIC blend films was quantified through grazing-incidence small-angle X-ray scattering (GISAXS) measurements, with the 2D images shown in Figures 5D–5F and the 1D profiles at the specular beam position within the region $q_z = 0.03 \pm 0.002 \text{ Å}^{-1}$ plotted in Figure 5I. In polymer:fullerene blend systems, the scattering intensity in the low q range comes from the polymer-rich domain and that in the high q range is attributed to the fractal-like fullerene aggregations.[45,46] To assist the 1D profile fitting of the non-fullerene blend film, we also obtained GISAXS patterns of pure PTB7-Th, and the 1D profiles are shown in Figure S3. It is observed that the signal of pure CO*i*8DFIC dominates the low q range from 0.004 to 0.02 Å^{-1}, while the signal from pure PTB7-Th governs the high q range from 0.02 to 0.1 Å^{-1}. The GISAXS scattering characteristics of PTB7-Th:CO*i*8DFIC are in startling contrast to the fullerene-based photovoltaic system. When PTB7-Th and CO*i*8DFIC were blended, the scattering intensity in the low q range increased a lot, due to the enhanced scattering contrast of the crystalline CO*i*8DFIC dispersed in the amorphous PTB7-Th:CO*i*8DFIC matrix. The scattering intensity in the high q range, on the other hand, does not show any significant changes, suggesting that CO*i*8DFIC molecules did not form fractal aggregates like its fullerene counterpart. The GISAXS scattering intensity in the 1D profiles of the PTB7-Th:CO*i*8DFIC blend can be attributed to (1) scattering contrast of crystalline CO*i*8DFIC relating to the amorphous PTB7-Th:CO*i*8DFIC matrix and (2) scattering contrast between PTB7-Th and CO*i*8DFIC molecules. We have applied two Debye-Anderson-Brumberger models to fit the large-scale and small-scale structures in the blend films.[45] The quantified domain sizes are summarized in Table 2. Here, correlation length (ζ_1) representing the large-scale structure (see Figure 5J) can be roughly regarded as the size of the amorphous PTB7-Th:CO*i*8DFIC domain. Meanwhile the correlation length (ζ_2) representing the small-scale structure is regarded as the distance between PTB7-Th and CO*i*8DFIC molecules in the amorphous PTB7-Th:CO*i*8DFIC domain. ρ_1 and ρ_2 are the relative volume fraction of ζ_1 and ζ_2. GISAXS fitting suggests that the blend film cast at RT comprises 33% large-scale structures and 67% small-scale structures. When the blend film was cast at RT with further SA treatment, the domain size of amorphous

Table 2. Fitting Parameters of 1D GISAXS Profiles of PTB7-Th:CO*i*8DFIC Films with Different Processing Methods

PTB7-Th:CO*i*8DFIC	ζ_1 (nm)	ρ_1 (%)	ζ_2 (nm)	ρ_2 (%)
Cast at RT	25.4	33	2.5	67
Cast at RT + SA	19.4	55	3.0	45
Cast on 100°C HS	24.6	14	2.4	86

PTB7-Th:CO*i*8DFIC (ζ_1) decreased from 25.4 to 19.4 nm due to the increased size of CO*i*8DFIC crystallites, and the volume fraction of these large-scale structures increased to 55%. In distinct contrast, casting the blend film on 100°C HS reduces the molecular organization time and restrains the growth of CO*i*8DFIC crystals, exhibiting decreased ρ_1 although the domain size of the amorphous region is slightly reduced at 24.6 nm.

Exciton Dissociation, Charge Transport, and Recombination

We proceeded to evaluate the exciton dissociation, charge transport, and recombination in these OPVs. Figure S4 shows the photocurrent density (J_{ph}) as a function of the effective voltage (V_{eff}). Here the J_{ph} of all OPVs saturates at large V_{eff}, indicating that all photogenerated excitons have dissociated into free carriers and all carriers are collected by the electrodes without any recombination. As shown in Table 3, their saturated short-circuit current densities (J_{sat}) are consistent with their EQE spectra. With the EQE spectrum being broadened, the J_{sat} became higher. The J_{ph}/J_{sat} value under short-circuit condition represents the exciton dissociation efficiency (P_{diss}), while the J_{ph}/J_{sat} value under the maximal power output condition represents the charge transport and collection efficiency (P_{coll}).[47] We found that the device cast on 100°C HS possesses the highest exciton dissociation efficiency and charge transport and collection efficiency, which is in line with its best device performance. The fact that both donors and acceptors are aligned in a face-on orientation, and the formation of intimate contact between them, account for the efficient exciton dissociation and charge transport.

Table 3 also shows the hole (μ_h) and electron (μ_e) motilities extracted from dark *J-V* curves of hole-only and electron-only devices (Figure S5). Encouragingly, when CO*i*8DFIC molecules change from the crystalline state (device cast at RT with SA) to the π-π stacked state (device cast on 100°C HS), its μ_e increased 4-fold and, although μ_h decreased slightly, the ratio of μ_h/μ_e is lowest at 2.1. We attribute the enhanced μ_e to J-type π-π stacking, which forms a long conjugated pathway for charge transport. The device cast on 100°C therefore obtained the most balanced charge mobility, whereas the ratios for those cast at RT or subjected to further SA are 10.3 and 14.8, respectively. To gain more insight into the charge recombination mechanism,[48] we studied the V_{oc} versus $\ln(P_{light})$ and $\log(J_{sc})$ versus $\log(P_{light})$. A slope close to 1 was obtained in the J_{sc} versus light intensity plots, suggesting very low bimolecular recombination in these devices. Slopes of 1.28, 1.28, and 1.13 kT/*q* were obtained in the V_{oc} versus light intensity plots for the devices cast at RT, at RT with SA, and on 100°C HS, respectively (see Figure S6A), suggesting that bimolecular recombination operates in all devices and the trap-assisted recombination became weaker in devices cast on HS.

Device Storage Lifetime

The storage lifetime of PTB7-Th:CO*i*8DFIC OPV devices fabricated using these different methods, and then encapsulated with epoxy glue and glass slides, was compared by storing devices in ambient conditions (with an average humidity of

Table 3. J_{sat}, P_{diss}, P_{coll}, and Electron and Hole Mobilities of PTB7-Th:COi8DFIC OPVs Prepared Using Different Processing Methods

|	J_{sat} (mA cm^{-2})	P_{diss} (%)	P_{coll} (%)	Hole Mobility (μ_h) (cm^2 V^{-1} s^{-1})	Electron Mobility (μ_e) (cm^2 V^{-1} s^{-1})	μ_h/μ_e
Cast at RT	25.9	95.6	75.4	$(8.5 \pm 2.0) \times 10^{-4}$	$(0.82 \pm 0.2) \times 10^{-4}$	10.3
Cast at RT + SA	21.9	92.6	70.1	$(7.8 \pm 1.6) \times 10^{-4}$	$(0.54 \pm 0.2) \times 10^{-4}$	14.8
Cast on 100°C HS	28.6	96.6	83.2	$(5.1 \pm 1.5) \times 10^{-4}$	$(2.39 \pm 0.5) \times 10^{-4}$	2.1

70% and temperature of 25°C), and testing them periodically to obtain the photovoltaic parameters. As shown in Figure 6, the V_{oc} and FF of all devices exhibit similar variations during 30 days of storage in air, with the V_{oc} almost unchanged and FF decreasing by ~10%. The J_{sc} of the device cast at RT with further SA treatment is reduced by 10% after storing for 30 days, but the J_{sc} of other two devices are not altered during the storing period. Eventually, the device cast at RT with further SA treatment (featuring edge-on and flat-on crystal structure) loses 20% PCE and the other two retain about 90% of the original PCE. As reported in previous work, PTB7-Th-based OPV devices possess inferior environmental stability due to their easily oxidized alkoxy-benzo[1,2-b:4,5-b']dithiophene unit,[49,50] manifesting declined J_{sc} over time by storing devices in air for days. We believe that the instability of PTB7-Th contributes to a large part of the performance degradation of PTB7-Th:COi8DFIC OPVs. The fact that larger PTB7-Th domains exist in the device cast at RT with further SA treatment may account for its faster degradation rate. Nevertheless, our investigation illuminates that COi8DFIC molecules with a lower degree of crystallization present longer storage lifetime, and demonstrate promising merit by pairing with an efficient and stable electron donor. We also note that HS casting can be adopted during the large-scale roll-to-roll device fabrication process.

In summary, we have demonstrated an effective strategy to improve device efficiency and lifetime via molecular order control of PTB7-Th:COi8DFIC non-fullerene OPVs. Prolonged molecular organization time will promote flat-on and edge-on lamellar COi8DFIC crystallization and leads to large-scale phase separation between PTB7-Th and COi8DFIC, resulting in inefficient exciton dissociation and poor charge-transport properties. However, reducing the molecular organization time by film-casting on an HS is efficient in suppressing the crystallization and promotes both H- and J-type face-on π-π stacking of COi8DFIC molecules in a more condensed state. The favorable morphology obtained via HS casting not only improved light absorption at long wavelength and exciton dissociation but also enhanced electron mobility to achieve the balanced carrier mobility. As a result, a notable PCE$_{max}$ of 13.8% was achieved in the binary PTB7-Th:COi8DFIC non-fullerene OPVs, while also exhibiting superior storage stability when the conformation of COi8DFIC is face-on π-π stacking. Our results provide comprehensive guidance for optimizing the molecular order, orientation, and nanoscale morphology of non-fullerene-based OPVs, especially those employing highly crystallizable NFAs as the electron acceptor.

EXPERIMENTAL PROCEDURES

Device Fabrication

COi8DFIC was synthesized in our previous work.[27] PTB7-Th was purchased from Solarmer Materials (Beijing). ZnO precursor solution was prepared according to a previous literature report.[51] All solar cells were fabricated in an inverted structure. The prepatterned ITO-glass substrates (resistance ca. 15 Ω per square) were cleaned by sequential sonication in water, ethanol, and isopropyl alcohol for 10 min each, before drying at 100°C on a hotplate. These substrates were further treated with
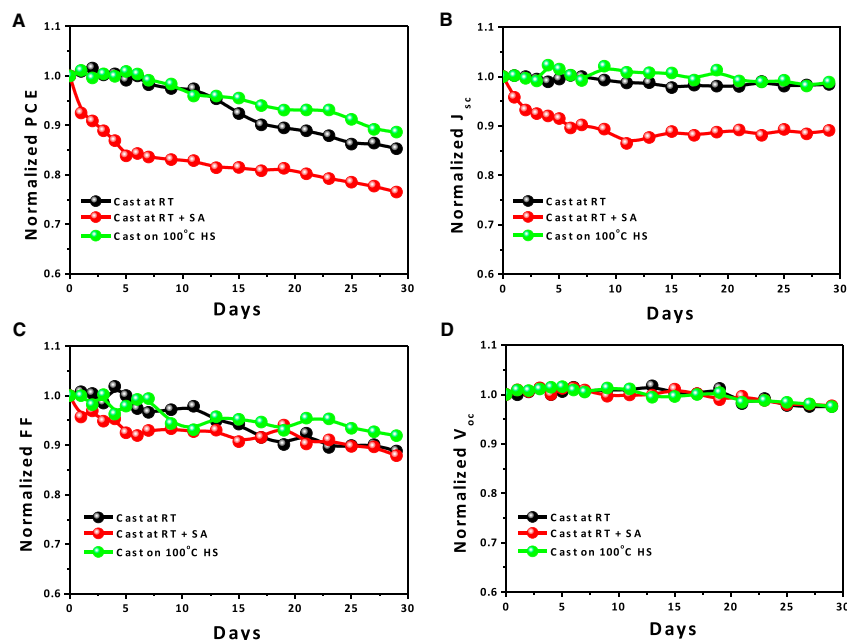
Figure 6. Storage Lifetime of PTB7-Th:CO*i*8DFIC OPV Devices

(A–D) The evolutions of (A) PCE, (B) J_{sc}, (C) FF, and (D) V_{oc} over storage time for encapsulated PTB7-Th:CO*i*8DFIC OPV devices fabricated using different processing methods.

UV/ozone for 10 min before solution processing. ZnO films, 30 nm thick, were spin-coated onto cleaned ITO substrates, then dried at 200°C for 30 min in air. The photoactive layer was then deposited on top of the ZnO layer by spin-coating from a 16 mg/mL chlorobenzene solution (with 1 vol% 1,8-diiodooctane) of PTB7-Th:CO*i*8DFIC to obtain films of 100 nm thickness, in a nitrogen-filled glove-box. For devices cast on HS, the ITO/ZnO substrates were preheated on a hotplate at RT, 50°C, 70°C, 100°C, and 150°C before spin-coating. To achieve similar thickness of the active layer at 100 nm, we set the spin speed for temperatures of substrate at RT, 50°C, 70°C, 100°C, and 150°C to 700, 900, 1,100, 1,300, and 1,500 rpm, respectively. For the device treated with solvent annealing, the as-cast film was transferred into a glass chamber, containing a reservoir with an excess of CB, resulting in a saturated CB solvent-vapor atmosphere, for 1 min. Thereafter, 10 nm of MoO_3 and 100 nm of Ag were thermally evaporated, forming the anode and counter electrode under high vacuum to finish the device preparation. The size of the photoactive area defined by the overlapping of anode and cathode is 4 mm^2.

Characterization

Film absorption spectra were measured using a UV-visible spectrophotometer (Lambda750, PerkinElmer, USA). Film thickness was measured using a spectroscopic ellipsometer (J.A. Woollam, USA). The surface morphologies of the active layers were characterized by a scanning probe microscope (NT-MDT, Russia) and a trans-mission electron microscope (JEOL, Japan). Device *J-V* characterization was per-formed under AM 1.5G (100 mW cm^{-2}) using a Sol3A solar simulator (Newport, USA) in air at RT. The light intensity was calibrated using a standard silicon reference cell certified by the National Renewable Energy Laboratory (USA). *J-V* characteristics were recorded using J-V Sweep software developed by Ossila (UK) and a 2612B (Keithley, USA) source meter unit. EQE was measured with a Zolix (China) EQE

system equipped with a standard Si diode. PL was obtained using a PL microscopic spectrometer (Flex One; Zolix, China) with a 532-nm continuous-wave laser as the excitation source. Synchrotron-based GIWAXS measurements were conducted at beamline I07 of the Diamond Light Source in the UK. Synchrotron-based GISAXS measurements were conducted using the beamline BL16B1 at the Shanghai Synchrotron Radiation Facility in China.

SUPPLEMENTAL INFORMATION

Supplemental Information includes Supplemental Experimental Procedures and six figures and can be found with this article online at https://doi.org/10.1016/j.joule.2018.11.023.

AUTHOR CONTRIBUTIONS

W.L. and T.W. conceived and developed the ideas. Z.X. and L.D. synthesized CO*i*8DFIC. W.L. and M.C. designed the experiments and performed device fabrication, electrical characterization, and data analysis. W.L., J.C., and H.Z. performed the lifetime measurements. T.W., W.L., R.S.G., J.C., E.L.K.S., and D.G.L. performed the GISAXS and GIWAXS measurements. W.L. and D.L. collected SPM and TEM data. All authors discussed the results. W.L. and T.W. wrote the manuscript. This project was directed by T.W. and L.D.

DECLARATION OF INTERESTS

The authors declare no competing interests.

REFERENCES

1. Cheng, P., Li, G., Zhan, X., and Yang, Y. (2018). Next-generation organic photovoltaics based on non-fullerene acceptors. Nat. Photon. *12*, 131–142.

2. Hou, J., Inganas, O., Friend, R.H., and Gao, F. (2018). Organic solar cells based on nonfullerene acceptors. Nat. Mater. *17*, 119–128.

3. Yan, C., Barlow, S., Wang, Z., Yan, H., Jen, A.K.Y., Marder, S.R., and Zhan, X. (2018). Non-fullerene acceptors for organic solar cells. Nat. Rev. Mater. *3*, 18003.

4. Lin, Y., Wang, J., Zhang, Z.G., Bai, H., Li, Y., Zhu, D., and Zhan, X. (2015). An electron acceptor challenging fullerenes for efficient polymer solar cells. Adv. Mater. *27*, 1170–1174.

5. Holliday, S., Ashraf, R.S., Wadsworth, A., Baran, D., Yousaf, S.A., Nielsen, C.B., Tan, C.H., Dimitrov, S.D., Shang, Z., Gasparini, N., et al. (2016). High-efficiency and air-stable P3HT-based polymer solar cells with a new non-fullerene acceptor. Nat. Commun. *7*, 11585.

6. Sun, J., Ma, X., Zhang, Z., Yu, J., Zhou, J., Yin, X., Yang, L., Geng, R., Zhu, R., Zhang, F., et al. (2018). Dithieno [3, 2-b: 2′, 3′-d] pyrrol fused nonfullerene acceptors enabling over 13% efficiency for organic solar cells. Adv. Mater. *30*, 1707150.

7. Li, S., Ye, L., Zhao, W., Liu, X., Zhu, J., Ade, H., and Hou, J. (2017). Design of a new small-molecule electron acceptor enables efficient

polymer solar cells with high fill factor. Adv. Mater. *29*, 1704051.

8. Cheng, P., Zhang, M., Lau, T.K., Wu, Y., Jia, B., Wang, J., Yan, C., Qin, M., Lu, X., and Zhan, X. (2017). Realizing small energy loss of 0.55 eV, high open-circuit voltage >1 V and high efficiency >10% in fullerene-free polymer solar cells via energy driver. Adv. Mater. *29*, 1605216.

9. Zhang, H., Yao, H., Hou, J., Zhu, J., Zhang, J., Li, W., Yu, R., Gao, B., Zhang, S., and Hou, J. (2018). Over 14% efficiency in organic solar cells enabled by chlorinated nonfullerene small-molecule acceptors. Adv. Mater. *30*, 1800613.

10. Zhao, J., Li, Y., Yang, G., Jiang, K., Lin, H., Ade, H., Ma, W., and Yan, H. (2016). Efficient organic solar cells processed from hydrocarbon solvents. Nat. Energy *1*, 15027.

11. Ye, L., Zhao, W., Li, S., Mukherjee, S., Carpenter, J.H., Awartani, O., Jiao, X., Hou, J., and Ade, H. (2017). High-efficiency nonfullerene organic solar cells: critical factors that affect complex multi-length scale morphology and device performance. Adv. Energy Mater. *7*, 1602000.

12. Li, H., Zhao, Y., Fang, J., Zhu, X., Xia, B., Lu, K., Wang, Z., Zhang, J., Guo, X., and Wei, Z. (2018). Improve the performance of the all-small-molecule nonfullerene organic solar cells through enhancing the crystallinity of acceptors. Adv. Energy Mater. *8*, 1702377.

13. Song, X., Gasparini, N., Ye, L., Yao, H., Hou, J., Ade, H., and Baran, D. (2018). Controlling blend morphology for ultrahigh current density in nonfullerene acceptor-based organic solar cells. ACS Energy Lett. *3*, 669–676.

14. Ye, L., Collins, B.A., Jiao, X., Zhao, J., Yan, H., and Ade, H. (2018). Miscibility-function relations in organic solar cells: significance of optimal miscibility in relation to percolation. Adv. Energy Mater. *8*, 1703058.

15. Li, W., Cai, J., Yan, Y., Cai, F., Li, S., Gurney, R.S., Liu, D., McGettrick, J.D., Watson, T.M., Li, Z., et al. (2018). Correlating three-dimensional morphology with function in PBDB-T: IT-M non-fullerene organic solar cells. Solar RRL *2*, 1800114.

16. Ye, L., Jiao, X., Zhou, M., Zhang, S., Yao, H., Zhao, W., Xia, A., Ade, H., and Hou, J. (2015). Manipulating aggregation and molecular orientation in all-polymer photovoltaic cells. Adv. Mater. *27*, 6046–6054.

17. Adil, M.A., Zhang, J., Deng, D., Wang, Z., Yang, Y., Wu, Q., and Wei, Z. (2018). Modulation of the molecular orientation at the bulk heterojunction interface via tuning the small molecular donor-nonfullerene acceptor interactions. ACS Appl. Mater. Interfaces *10*, 31526–31534.

18. Gregg, B.A. (2011). Entropy of charge separation in organic photovoltaic cells: the benefit of higher dimensionality. J. Phys. Chem. Lett. *2*, 3013–3015.

19. Li, W., Cai, J., Cai, F., Yan, Y., Yi, H., Gurney, R.S., Liu, D., Ahmed, I., and Wang, T. (2018). Achieving over 11% power conversion efficiency in PffBT4T-2OD-based ternary polymer solar cells with enhanced open-circuit-voltage and suppressed charge recombination. Nano Energy *44*, 155–163.

20. Rajaram, S., Shivanna, R., Kandappa, S.K., and Narayan, K.S. (2012). Nonplanar perylene diimides as potential alternatives to fullerenes in organic solar cells. J. Chem. Phys. Lett. *3*, 2405–2408.

21. Hu, H., Li, Y., Zhang, J., Peng, Z., Ma, L.K., Xin, J., Huang, j., Ma, T., Jiang, K., Zhang, G., et al. (2018). Effect of ring-fusion on miscibility and domain purity: key factors determining the performance of PDI-based nonfullerene organic solar cells. Adv. Energy Mater. *8*, 1800234.

22. Zhao, J., Tan, H.S., Guo, X., Facchetti, A., and Yan, H. (2018). Material insights and challenges for non-fullerene organic solar cells based on small molecular acceptors. Nat. Energy *3*, 720–731.

23. Baran, D., Kirchartz, T., Wheeler, S., Dimitrov, S., Abdelsamie, M., Gorman, J., Ashraf, R.S., Wadsworth, A., Gasparini, N., Kaienburg, P., et al. (2016). Reduced voltage losses yield 10% efficient fullerene free organic solar cells with >1 V open circuit voltages. Energy Environ. Sci. *9*, 3783–3793.

24. Eastham, N.D., Dudnik, A.S., Aldrich, T.J., Manley, E.F., Fauvell, T.J., Hartnett, P.E., Wasielewski, M.R., Chen, L.X., Melkonyan, F.S., Facchetti, A., et al. (2017). Small molecule acceptor and polymer donor crystallinity and aggregation effects on microstructure templating: understanding photovoltaic response in fullerene-free solar cells. Chem. Mater. *29*, 4432–4444.

25. Bin, H., Yang, Y., Peng, Z., Ye, L., Yao, J., Zhong, L., Sun, C., Gao, L., Huang, H., Li, X., et al. (2018). Effect of alkylsilyl side-chain structure on photovoltaic properties of conjugated polymer donors. Adv. Energy Mater. *8*, 1702324.

26. Mai, J., Xiao, Y., Zhou, G., Wang, J., Zhu, J., Zhao, N., Zhan, X., and Lu, X. (2018). Hidden structure ordering along backbone of fused-ring electron acceptors enhanced by ternary bulk heterojunction. Adv. Mater. *30*, 1802888.

27. Xiao, Z., Jia, X., Li, D., Wang, S., Geng, X., Liu, F., Chen, J., Yang, S., Russell, T.P., and Ding, L. (2017). 26 mA cm^{-2} J$_{sc}$ from organic solar cells with a low-bandgap nonfullerene acceptor. Sci. Bull. *62*, 1494–1496.

28. Xiao, Z., Xue, J., and Ding, L. (2017). Ternary organic solar cells offer 14% power conversion efficiency. Sci. Bull. *62*, 1562–1564.

29. Li, H., Xiao, Z., Ding, L., and Wang, J. (2018). Thermostable single-junction organic solar cells with a power conversion efficiency of 14.62%. Sci. Bull. *63*, 340–342.

30. Meng, L., Zhang, Y., Wan, X., Li, C., Zhang, X., Wang, Y., Ke, X., Xiao, Z., Ding, L., Xia, R., et al. (2018). Organic and solution-processed tandem solar cells with 17.3% efficiency. Science *361*, 1094–1098.

31. Swick, S.M., Zhu, W., Matta, M., Aldrich, T.J., Harbuzaru, A., Navarrete, J.T.L., Ortiz, R.P., Kohlstedt, K.L., Schatz, G.C., Facchetti, A., et al. (2018). Closely packed, low reorganization energy π-extended postfullerene acceptors for efficient polymer solar cells. Proc. Natl. Acad. Sci. U S A *115*, E8341–E8348.

32. Wang, T., Pearson, A.J., and Lidzey, D.G. (2013). Correlating molecular morphology with optoelectronic function in solar cells based on

low band-gap copolymer:fullerene blends. J. Mater. Chem. C *1*, 7266–7293.

33. Li, G., Yao, Y., Yang, H., Shrotriya, V., Yang, G., and Yang, Y. (2007). "Solvent annealing" effect in polymer solar cells based on poly (3-hexylthiophene) and methanofullerenes. Adv. Funct. Mater. *17*, 1636–1644.

34. Wang, N., Zhan, L., Li, S., Shi, M., Lau, T.K., Lu, X., Shikler, R., Li, C.Z., and Chen, H. (2018). Enhancement of intra-and inter-molecular π-conjugated effects for a non-fullerene acceptor to achieve high-efficiency organic solar cells with an extended photoresponse range and optimized morphology. Mater. Chem. Front. *2*, 2006–2012.

35. Spano, F.C., and Silva, C. (2014). H- and J-aggregate behavior in polymeric semiconductors. Annu. Rev. Phys. Phys. Chem. *65*, 477–500.

36. Dai, S., Li, T., Wang, W., Xiao, Y., Lau, T., Li, Z., Liu, K., Lu, X., and Zhan, X. (2018). Enhancing the performance of polymer solar cells via core engineering of NIR-absorbing electron acceptors. Adv. Mater. *30*, 1706571.

37. Yao, H., Cui, Y., Yu, R., Gao, B., Zhang, H., and Hou, J. (2017). Design, synthesis, and photovoltaic characterization of a small molecular acceptor with an ultra-narrow band gap. Angew. Chem. Int. Ed. *56*, 3045–3049.

38. Li, W., Yan, Y., Gong, Y., Cai, J., Cai, F., Gurney, R.S., Liu, D., Pearson, A.J., Lidzey, D.G., and Wang, T. (2018). Contrasting effects of energy transfer in determining efficiency improvements in ternary polymer solar cells. Adv. Funct. Mater. *28*, 1704212.

39. Chen, Y., Ye, P., Zhu, Z.G., Wang, X., Yang, L., Xu, X., Wu, X., Tao, D., Zhang, H., Hou, J., et al. (2017). Achieving high-performance ternary organic solar cells through tuning acceptor alloy. Adv. Mater. *29*, 1603154.

40. Ye, L., Xiong, Y., Zhang, Q., Li, S., Wang, C., Jiang, Z., Hou, J., You, W., and Ade, H. (2018). Surpassing 10% efficiency benchmark for nonfullerene organic solar cells by scalable coating in air from single nonhalogenated solvent. Adv. Mater. *30*, 1705485.

41. Ma, W., Tumbleston, J.R., Wang, M., Gann, E., Huang, F., and Ade, H. (2013). Domain purity, miscibility, and molecular orientation at donor/acceptor interfaces in high performance organic solar cells: paths to further improvement. Adv. Energy Mater. *3*, 864–872.

42. Nguyen, T.Q., Doan, V., and Schwartz, B.J. (1999). Conjugated polymer aggregates in solution: control of interchain interactions. J. Chem. Phys. *110*, 4068–4078.

43. Liu, Y., Zhao, J., Li, Z., Mu, C., Ma, W., Hu, H., Jiang, K., Lin, H., Ade, H., and Yan, H. (2014). Aggregation and morphology control enables multiple cases of high-efficiency polymer solar cells. Nat. Commun. *5*, 5293.

44. Qian, D., Ye, L., Zhang, M., Liang, Y., Li, L., Huang, Y., Guo, X., Zhang, S., Tan, Z., and Hou, J. (2012). Design, application, and morphology study of a new photovoltaic polymer with strong aggregation in solution state. Macromolecules *45*, 9611–9617.

45. Liao, H.C., Tsao, C.S., Lin, T.H., Chuang, C.M., Chen, C.Y., Jeng, U.S., Su, C.H., Chen, Y.F., and Su, W.F. (2011). Quantitative nanoorganized structural evolution for a high efficiency bulk heterojunction polymer solar cell. J. Am. Chem. Soc. *133*, 13064–13073.

46. Wu, W.R., Jeng, U.S., Su, C.J., Wei, K.H., Su, M.S., Chiu, M.Y., Chen, C.Y., Su, W.B., Su, C.H., and Su, A.C. (2011). Competition between fullerene aggregation and poly (3-hexylthiophene) crystallization upon annealing of bulk heterojunction solar cells. ACS Nano 5, 6233–6243.

47. He, Z., Zhong, C., Huang, X., Wong, W.Y., Wu, H., Chen, L., Su, S., and Cao, Y. (2011). Simultaneous enhancement of open-circuit voltage, short-circuit current density, and fill factor in polymer solar cells. Adv. Mater. *23*, 4636–4643.

48. Proctor, C.M., Martijn, K., and Thuc-Quyen, N. (2013). Charge carrier recombination in organic solar cells. Prog. Polym. Sci. *38*, 1941–1960.

49. Li, N., and Brabec, C.J. (2015). Air-processed polymer tandem solar cells with power conversion efficiency exceeding 10%. Energy Environ. Sci. *8*, 2902–2909.

50. Lu, L., and Yu, L. (2013). Understanding low bandgap polymer PTB7 and optimizing polymer solar cells based on it. Adv. Mater. *26*, 4413–4430.

51. Sun, Y., Seo, J.H., Takacs, C.J., Seifter, J., and Heeger, A.J. (2011). Inverted polymer solar cells integrated with a low-temperature-annealed sol-gel-derived ZnO film as an electron transport layer. Adv. Mater. *23*, 1679–1683.